Application of micro X-ray fluorescence to chemical mapping of polar ice.

Morel Fourcade M.C.[1], Barnola J.M. [1], Susini J[2], Baker R. [2], Durand G. [1], de Angelis M. [1], Duval P. [1]

[1] LGGE, BP96, 38402 Saint Martin d'Hères, France, [2]ESRF, BP 220 38043 Grenoble, France

Abstract:

Synchrotron based micro X-ray fluorescence (μXRF) equipment has been used to analyse impurities in polar ice. A customised sample holder has been developed and the μXRF equipment has been adapted with a thermal control system to keep samples unaltered during analyses. Artificial ice samples prepared from ultra pure water were analysed to enable the detection of contamination or experimental artifacts. Analyses of polar ice from Antarctica, - Dome C and Vostok – confirm this μXRF technique is non-destructive and sensitive. Experiments can be reproduced to confirm or refine results by focusing on interesting spots such as crystal boundaries or specific inclusions. Integration times and resolution can be adjusted to optimise sensitivity. Investigation of unstable particles is possible due to the short analysis time. In addition to identification of elements in impurities μ-XRF determines their speciations. The accuracy and reliability of results confirm the potential of this technique for research in glaciology.

1 INTRODUCTION

Studying impurities in ice is essential for current research in glaciology. Issues that have to be addressed for analysis of ice cores come from the fragility of the ice material, its evolving structure, and the low concentrations of impurities.

Analysis of melted samples by ion chromatography gives the average ionic concentrations of soluble (mineral and organic) species, even at very low concentrations. Such information is used for studying past atmospheric composition, for example. However, due to the possible interaction between chemical impurities and physical properties it is of primary interest to know the micro-structural localization of impurities. Depending on their localization, either dispersed in the ice matrix or concentrated at grain boundaries, the structure of the sample may evolve from its original *in-situ* state. For example: reactions between the soluble sulphuric acid and carbonate particulates may alter the record of atmospheric CO_2 present in air bubbles trapped in the ice (Legrand and Mayeswski, 1997).

Several analytical methods have already been successfully developed to locate impurities in ice (Baker and others, 2003) or to study their effect on properties of ice (Wolff and Mulvaney, 1988; Iliescu and others, 2003). Acidic ions at a triple junction of Antarctic ice have been studied by the Raman scattering technique (Fukazawa and others, 1998). Trickett and others (2000) studied the effect of H_2SO_4 on mechanical properties of ice by synchrotron X-ray topography. The major technique implemented to observe impurities is scanning electron

microscopy (SEM) with energy dispersive X-ray microanalysis (EDS). Mulvaney and others (1988) found sulphuric acid at the grain boundaries in Antarctic ice. In the last few years, two teams have successfully developed this technique (Barnes and other, 2002, 2003; Cullen and Baker, 2002).

Whilst sublimation concentrates impurities and facilitates detection, it may also introduce artifacts: for example filaments observed in the grain boundaries of polar ice are due to the sublimation of the surrounding ice (Baker and Cullen, 2003). Developing a new experimental method that enables mapping and analysis of impurities in a non-destructive way is seen as valuable for research in glaciology.

To this end we looked at the X-ray microscopy analysis technique developed at the ID21 beamline at the European Synchrotron Radiation Facility (ESRF) in Grenoble, France (Susini and others, 2002). This technique enables the investigation of hydrated frozen samples without any pre-treatment. It allows study of thick samples, and in the high energy range produced by this technique, fluorescence yield is high enough to be mapped with significant contrast and to identify low Z elements. With these capabilities the µXRF technique appears a suitable basis from which a new experimental method could be built for mapping and analyzing impurities in a non invasive way. In this paper we report the technical and methodological adaptations implemented, the validation of the technique, and the first results obtained.

2 EXPERIMENTAL PROCEDURE

2.1 Equipment

An analysis chamber (internal part shown on Fig. 1a) is closed by a tight door, as a high vacuum (~ 10^{-5} mbar) is necessary to lower the detection limit and to have access to low Z elements.

To preserve the ice sample from any transformation or sublimation it must be maintained at low temperature (~ 120 K during analysis). The cooling system consists of a special 3 litre Dewar (Fig. 1a (a)), automatically filled with liquid nitrogen (LN_2) and hermetically fixed to the roof of the chamber by a DN100 flange. The base of the Dewar is made of a thick copper cylinder (Fig. 1a (b)) coupled to a magnetized copper plate by a flexible copper tress (Fig. 1a (c) and Fig. 1c), the sample cell being fixed to this plate by magnets. This maintains the ice sample temperature near the same low temperature as the bottom of the Dewar. A thermocouple is fixed on the copper plate to measure the temperature during experiments (Fig. 1a (d)). The upper part of Figure 1b shows the front window (a) of the cell in which the sample is set up. The window is a transparent film of Ultralene®. Ultralene® was selected for its good X-ray transmission, its strength and purity. The film is pressed between the lid and the sample cell (Fig. 1c) with a Viton O-ring to ensure air-tightness. The sample cell is thermally isolated from its support by Peek® pieces (Fig. 1b (c)). The sample cell and its support are made of aluminium. Magnets (Fig. 1b (e)) fix the support on a steel plate which holds the whole sample set device. A piezometer based scanner (Fig. 1a (e)) moves the support of the sample cell by steps along x and y. Steps are adjustable according to

the lateral resolution desired. To obtain a scan rapidly , the total mass of the sample cell device associated with the piezometer has to be lower than 100 g. Hence the choice of aluminium for the sample cell device.

2.2 Sample selection

i) Artificial samples

In order to estimate the contamination introduced by the sample preparation and to evaluate the background signal of the measurement procedure, one artificial ice sample (S1) was prepared from ultra-pure water.

ii) Natural samples

Samples should be selected that provide the opportunity to evaluate the technique regarding in particular, localization of impurities, analysis of large aggregates and speciation of elements. Two technical constraints must be dealt with: (i) the μXRF detection limit of the instrument, expected to be of about 1 ppm, required samples with a significant amount of impurities. (ii) the small size of the sample cell (diameter only 11mm) required ice with small crystals in order to observe several grain boundaries. Accordingly, EPICA DC samples, from the last glacial maximum, at 566 m depth, were selected. In addition samples of accreted ice from lake Vostok at about 3750 m depth were selected to analyze aggregates.

2.3 Sample preparation

Samples were prepared at LGGE, Grenoble, France in a cold room at 258 K. To prevent contamination, every tool was new and washed with methanol. Ice cores were cut into samples of 7 cm length. Each sample was machined to a cylinder with the same diameter as the sample cell. The surface of each cylinder was adjusted with a microtome to exactly fit in the cell and to be flush with the cell surface on which the Ultralene® film was spread. Once the sample cell was sealed with screws (Fig.1b,(d)), it was put into a polycarbonate box to avoid contamination of the Ultralene® film. Samples were then transferred to the ESRF at a temperature of 235 K and cooled to LN_2 just before introduction into the analysis chamber.

2.4 Sample set up in the analysis chamber

It is critical that water vapour be prevented from entering the chamber as this could turn into hoar on the cell window. For this reason, the chamber was put under a vacuum (~10^{-5} mbar). The Dewar was then filled with LN_2. Once the temperature of the copper plate lowered to 113 K, the analysis chamber was brought back to atmospheric pressure with dry N_2. Outside the chamber, at the level of the top of the door, a laminar flow of dry N_2 was blown downwards to keep humidity low in the chamber at the door aperture. The door was opened, the sample box removed from the LN_2, introduced into the chamber and opened. The sample cell and its support (Fig. 1b) were placed in the X-ray beam and fixed by magnets (Fig. 1b (e)). The copper plate and its tress were put in contact with the sample cell and the door was closed. The vacuum was re-pumped and the temperature became stable at 123

K after 1.5 h. The time duration for which the door was left open was less than one minute. The maximum temperature observed for the sample cell during set up was 203 K. There was no hoar in the chamber except for some traces on the copper tress.

2.5 Analysis

Initially, the surface of the polar ice sample was observed with an optical microscope in order to check the absence of hoar on the Ultralene® film, to verify that the ice was intact, and to identify grain boundaries. Once a grain boundary or an interesting spot was selected, the ice sample was examined using the X-ray microscopy beamline ID21 (Susini and others, 2002). The X-ray beam was focused down to a microprobe of 0.5 x 0.5 μm^2 by means of a Fresnel zone plate (Di Fabrizio and others, 1999). Two Si <111> crystals provided a monochromatic beam ($\Delta E/E = 10^{-4}$). The fluorescence signal was analyzed using a high energy resolution Germanium solid state detector. The incident beam energy was fixed at either 4500 eV to ensure a good fluorescence yield for elements ranging from calcium to sulfur. For sulfur speciation, the excitation beam was tuned at energy of 2482 eV. For both configurations, 4500 eV and 2482 eV, the probed depth (z axis) is 50 and 25 µm respectively. The lateral resolution, defined by the geometric projection of the focused beam onto the sample (x and y axes), was adapted to the size of the image and ranged from 3 x 3μm^2 to 0.5 x 0.5μm^2. The integration time, tuned from 100 ms/pixel and 5s /pixel, was determined by both concentration of the emitting elements and signal-to-noise ratio of the fluorescence signal.

Ice adjacent to the samples was analyzed by ion chromatography in order to get the average concentrations of the main ionic species of the melted ice (Table 1) (Saigne and others, 1987). The concentrations ranged from 0.13 to 938 ppb.

3 RESULTS AND DISCUSSION

3.1 Technique validation

i) Blank of the experimental procedure and background estimation

To estimate the contamination introduced by the sample preparation and to test the influence of the Ultralene® film, two XRF spectra (Fig. 2) were drawn under the same experimental conditions as for the polar ice samples: one using a sample cell filled with air and the other using an artificial sample (S1), which was also analyzed by ion chromatography (see Table 1). To take account of the variations of the incoming intensity (Io) during experiments, all the figures presented in this paper show the relative intensity, i.e. the ratio (I/Io) of the emitted signal (I) to the incoming intensity. The results for both the air-filled cell and S1 (Table 2) are similar for the chloride peak. Because Cl was not detected by ion chromatography of S1, the Ultralene® film, which is very close to the sample surface is most likely the source of the Cl peak.

Regarding elements other than Cl (Table 2), the Al peak was lower for S1 than for the cell filled with air. This may be due to the partial absorption of the cell signal by the S1 sample. It was decided that the μXRF signal for an element in S1 would

be taken as the background signal. To consider an element as present in polar ice, the µXRF signal should be more than two times higher than the element's signal in S1.

ii) Sample conservation during the experiment.

The major risk of transformation of samples is sublimation. Sublimation can be due to a lack of closure of the sample cell in the vacuum chamber. Figure 2 shows the µXRF spectrum for the sample cell filled with air: there is a high peak for argon. Although present as traces in air, Ar has been detected due to its atomic number (18) which explains its good fluorescence response. This Ar peak confirms the air-tightness of the sample cell.

To check both the stability of the sample and the reproducibility of the technique, a inclusion containing Si in the Vostok sample -depth 3572m- (V2) has been examined three times at intervals of 2 h 30 minutes. The µXRF spectra – only Si Kα line relative intensity - and shape of the Si peaks along the cross section of the inclusion are shown on Figures 3a and 3b. Whilst the shape of the inclusion is kept unchanged (Fig.3b), a slight decrease of I/Io is observed (Fig 3a). This suggests a slow evolution of the sample. The decrease is limited at about 20% after more than 7 hours. This confirms the experiment is non destructive and can be reproduced.
Several experiments were carried out on the same part of an inclusion containing Cl in the Vostok sample- depth 3572m- (V1). From optical microscopy, this inclusion appears like a spherical grain (2µm). Table 3 shows the stability of I/Io

for Cl in this inclusion after use of different integration times. This stability means that integration times can be increased -at least up to 5s- to improve the sensitivity of the technique without causing elemental repartition. Between each scan, examinations by optical microscopy were made showing that the inclusion was unchanged and that the surface of the sample was not altered by the radiation from the microscope.

3.2 First results

Results from DC1 -566m depth

The observation of sample DC1 by optical microscopy shows an homogeneous surface apart from the grain boundary. The total area mapped by µXRF was of 200 x 188 μm^2 with a pixel size of 2.6 (x) x 2.6 (y) μm^2, an integration time of 3.3 s, and an exciting energy of 4500 eV. Note that the signal include information from a thickness of about 50 µm below each pixel. The K map (Fig. 4a) shows a strong concentration of K along the grain boundary. This result is observed under the non-destructive conditions of the technique. This can be explained by the concept that K, which in most cases is in an easily soluble form, should be preferentially found along the grain boundaries or associated with insoluble particles. Other elements such as Si, Al, S and, Ca were also detected. However instead of being, as K, highly concentrated in a continuous area, they are either concentrated only on a few points or distributed in a rather homogeneous way throughout the mapped area. As a result their maps show either a few dark points or a grey area without contrast. This is why, instead of their maps, we show their relative intensity profiles in three selected regions of the map identified as Z1, Z2 and Z3 (Fig. 4b).

The I/Io signal for Si, Al, Ca and K is < 0.04 except from specific spots. For example, Ca is present in specific spots such as point A and point B close to the triple junction (Fig. 4a and 4b), and point C. Except for a very intense point (A on Fig. 4a; I/Io~16), the signal for S (Fig. 4b; Z2, Z3) is about 4 times higher than the I/Io signal for the other elements. The origin of S is likely to be H_2SO_4 throughout the matrix. The intense point may originate from an insoluble particle of $CaSO_4$. Owing to the long integration time of 3.3 s, and in spite of the sensitivity for Si and Al is lower for Ca, it is noteworthy that Si and Al were detected at point A, B and C.

Results from Vostok samples V1 and V2

The V1 sample (3551m depth) shows very large crystals (Duval and others, 1998; Jouzel and others, 1999) with some inclusions visible by optical microscopy and a large aggregate visible to the naked eye (Fig. 5a). Such an aggregate, not observed in normal glacier ice, is formed by concentration and compression of very small particles locally accumulated during the accretion of ice. The gas around the aggregate was initially at ~ 300 bar making the aggregate very unstable. To make use of the non-destructive character of the technique, three adjacent elemental maps were drawn. The area of each map was 100 x 100 μm^2, with a pixel size of 1 (x) x 1 (y) μm^2, an integration time of 0.5 s, resulting in 1.5 h per map. Note that the signal include information from a thickness of about 50 µm below each pixel.

Figures 5b show the Ca map distributed as large particles (circles) of ~ 15 µm with their shapes and spectra being different inside and outside the aggregate (Fig. 5c). Inside the aggregate, Ca looks anti-correlated with K (Fig. 5b). Ca predominates outside the aggregate, probably within one $CaCO_3$ inclusion (dashed circle). Fearing that the aggregate disappeared due to its unstable state, several rapid scans - less than 1.5 h each – were made to capture the maximum information. S was observed as concentrated at the border and probably associated with Al, although it must be conceded that the sensitivity for Al was low. Work is being carried out to confirm and refine these results (submitted for publication by M. de Angelis, 2004).

Apart from the one large aggregate some visible inclusions were observed by optical microscopy, and then scanned. The signal intensity (I) for each element as well as its ratio (I/Io) to the intensity measured on the artificial sample S1 are reported in Table 4. Results for V1 are not significantly different than for S1. As ion chromatography of V1 had shown high concentrations of the species of interest (Table 1), this confirmed that the matrix was pure (de Angelis and others, 2004) and suggests that all impurities were strongly concentrated in inclusions. S was mainly in the aggregate V1 while Cl was in the inclusions in the form of NaCl.

It is noteable that by assessing the number of inclusions, their volumes and the volume explored in the map, a rough evaluation of NaCl concentration in the inclusions may be derived from the average concentration measured by ion chromatography.

The Vostok sample (V2) (3572m depth) was used to test the potential brought by the new technique to obtain speciation by selecting the energy of the incident beam according to the oxidation number of the target element. Absorption spectroscopy techniques are based on the measurement of the absorption coefficient of variation by tuning the energy of the probing photons through an absorption edge. This variation is physically related to the excitation cross-section of the core electrons into unoccupied electronic states or into vacuum continua. The spectral features observed close to the absorption edge – referred to as X-ray Absorption Near Edge Structure (XANES)- reflect the molecular environment of a given absorbing atom and provide the basic mechanism for imaging with chemical sensitivity (Stöhr,1992). Obtaining information on different chemical states within systems having the same elemental composition is possible (Cuif and others, 2003).

An observation was made of a spot showing a particle including Si, Al, P and S (Fig. 6). The size of the image is 50 x 40 μm^2, with a pixel size of 0.5 (x) x 0.5 (y), and an integration time of 0.5 s. Note that the signal include information from a thickness of about 25 µm below each pixel. The size of the particle is 20 x 13.5 μm^2. Figures 6a-c, respectively, show oxidized sulfur using an exciting energy of 2.482 keV, reduced sulfur using an exciting energy of 2.473 keV, and their different localizations. By supplying cartographies of elements for their different oxidation numbers, the technique yields information that can help to determine the sources of the impurities.

Conclusion

µXRF analyses of polar ice samples were carried out after adaptations of both equipment and methodology. Results obtained from Dome C and Vostok samples are the first results obtained from the technique. The thermal control system keeps ice samples unchanged during analysis. Integration times can be increased without alteration of samples. Sensitivity can be optimized by increasing integration times and, for a given beam energy, the set of identified elements is expanded. For a given time window, optimization results from a trade-off between integration time and resolution. For the selected samples, impurities were not altered by the analyses. As the elements within impurities were kept highly concentrated, they were detectable, although their average concentrations, measured on melted samples by ion chromatography are far beyond the detection limit of µXRF.

By selecting integration time, resolution and size of the area to be mapped, analyses times can be shortened to about 1 h which enables us to scrutinize unstable impurities. Being non-destructive, this µXRF technique makes it possible to reproduce experiments to confirm or refine results.

Beyond the detection of elements within impurities, the technique enables their speciations which may help with finding the origins of impurities. In conjunction with the technical adaptations, the use of artificial ice samples was included in the analysis process. By measuring background µXRF signals from artificial samples it was possible to detect artifacts or contamination due to experimental conditions.

Combined with the reproducibility of experiments, this brings reliability to the results and to the related forthcoming interpretations in glaciology.

Acknowledgment

We acknowledge the European Synchrotron Radiation Facility for providing the X-ray facilities ME481 and CH1568, and the EPICA and Vostok programs for ice samples. We thank Murielle Salomé for assistance on beamline ID21, R. Pieritz for help during the experiment and C. David, T. Weitkamp (Paul Scherrer Institute, Switzerland) and E. Di Fabrizio (INFM, Trieste, Italy) for providing zone plates. We thank Sonia Nagorski for improvements to our English writing.

REFERENCES

Baker, I. and D.Cullen. 2003. SEM/EDS observations of impurities in polar ice: artifacts or not ? *J. Glaciol*., **49**(165), 184-190.

Baker, I., D. Cullen and D. Iliescu. 2003. The microstructural location of impurities in ice. *Can. J. Phys*., **81**, 1-9.

Barnes, P.R.F., R. Mulvaney, E.W. Wolff and K. Robinson. 2002. A technique for the examination of polar ice using the scanning electron microscope. *J. Microsc.*, **205** (2), 118-124.

Barnes, P.R.F., E. W.Wolff, D.C. Mallard and H.M. Mader. 2003. SEM Studies of the Morphology and Chemistry of Polar Ice. *Microsc. Res. Techn.*, **62**, 62-69.

Cullen, D., I. Baker. 2002. Observation of sulfate crystallites in Vostok accretion ice. *Materials Characterization*, **48**, 263-269.

Cuif, J.P., Y. Dauphin, J. Doucet, M. Salome and J. Susini. 2003. XANES mapping of organic sulfate in three scleractinian coral skeletons, *Geochimica & Cosmochimica Acta*, 67(1), 75-83

de Angelis, M., J.-R. Petit, J. Savarino, R. Souchez and M.H. Thiemens. 2004. Contributions of an ancient evaporitic-type reservoir to subglacial Lake Vostok chemistry. *Earth Planet. Sci. Lett.*, **222**, 751-765.

Di Fabrizio, E., F. Romanato, M. Gentili, S. Cabrini, B. Kaulich, J. Susini and R. Barrett. 1999. High – efficiency multilevel zone plates for keV X-rays. *Nature*, **401** (89), 895-898.

Duval, P., V. Lipenkov, N.I. Barkov and S. de la Chapelle. 1998. Recrystallization and fabric development in the Vostok ice core. *EOS, **79**, AGU Fall Meeting, F152*

Fukazawa, H., K. Sugiyama, S. Mae, H. Narita and T. Hondoh. 1998. Acid ions at triple junction of Antarctic ice observed by Raman scattering. *Geophys. Res. Lett.*, **25**(15), 2845-2848.

Iliescu, D., I. Baker and X. Li. 2003. The effects of sulfuric acid on the creep, recrystallization, and electrical properties of ice. *Can. J. Phys.*, **81**, 395-400.

Jouzel, J., J.-R. Petit, R. Souchez, N. I. Barkov, V. Ya. Lipenkov, D. Raynaud, M. Stievenard, N.I. Vassiliev, V. Verbeke and F. Vimeux. 1999. More than 200 Meters of lake ice above subglacial Lake Vostok, Antarctica, *Science*, **286**, 2138-2141.

Legrand, M. and P. Mayeswski. 1997. Glaciochemistry of polar ice cores: A review. *Rev. Geophys*., **35**(30), 219-243.

Mulvaney, R., E.W. Wolff and K. Oates. 1988. Sulphuric acid at grain boundaries in Antarctic ice. *Nature*, **331**, 247-249.

Saigne, C., S. Kirchner and M. Legrand. 1987. Ion-chromatographic measurements of ammonium, fluoride, acetate, formate and methanesulphonate ions at very low levels in Antarctic ice. *Anal. Chim. Acta*, **203**, 11-21.

Stöhr, M., 1992, *NEXAFS Spectroscopy*, Berlin: Springer-Verlag.

Susini, J., M. Salomé, B. Fayard, R. Ortega and B. Kaulich. 2002. The scanning X-Ray Microprobe at the ESRF " X-Ray Microscopy" beamline. *Surf. Rev. and Lett.*, **9**(1), 203-211.

Trickett, Y.L., I. Baker and P.M.S. Pradhan. 2000. The effects of sulfuric acid on the mechanical properties of ice single crystals. *J. Glaciol.*, **46**(153), 239-243.

Wolff, E. W. and R. Mulvaney. 1988. The location of impurities in Antarctic ice. *Ann. Glaciol.*, **11**, 194-197.

Tables

Table 1: Concentrations (ng g^{-1}) measured by ion chromatography for each sample.

	Ca^{2+}	K^{+}	Cl^{-}	MSA	SO_4^{2-}	Si^{2+}	Al^{3+}	Mg^{2+}	Na^{+}	F^{-}	NO_3^{-}	NH_4^{+}
S1	0.87	0.28	-	-	0.30	-	-	0.13	0.35	0.29	-	0.21
DC1	2.34	1.30	15.35	1.22	80.5			2.61	20.4	0.70	14.4	-
V1	94.9	5.00	938	-	215	-	-	0.21	798	3.13	1.73	1.71
V2	14.6	9.00	721	-	44.1	-	-	4.51	623	2.33	1.97	0.45

Notes: no visible aggregate in V1 and V2. -: not detected

Table 2: µXRF results from test samples (artificial ice (S1) and sample cell filled with air).

	Ca	K	Cl	S	Si	Al	Mg	Na	F
Energy (keV)	3.69	3.31	2.62	2.31	1.74	1.48	1.25	1.04	0.67
I/Io S1	3.64	0.36	10.52	2.03	1.23	0.91	0.27	0.15	2.82
I/Io sample cell filled with air	3.20	0.80	15.15	1.59	2.40	3.20	-	-	2.40
	0.88	***2.22***	***1.44***	***0.78***	***1.95***	***3.52***	***-***	***-***	***0.85***

Notes: The Energy (keV) corresponds to the Kα emission line. Relative intensity of signal ($x10^8$), I/Io where I is the signal emitted by the element and Io the incoming intensity. In italic bold characters: ratio of the relative intensity to background (as measured on S1). Values lower than 2.0 are not considered significant. -: not detected

Table 3: Evolution of Cl relative intensity in an aggregate for different integration times.

	Integration time (s)	Relative intensity ($x10^8$)
Scan1	1	234
Scan2	0.1	236
Scan 3	5	242

Notes: The relative intensity of Cl in the ice apart from the aggregate is 10.5×10^{-8}. An estimation of the standard deviation of the relative intensity (234×10^{-8} to 242×10^{-8}) in this aggregate is $\pm$ 70 x 10^{-8}. Between scan 1 and scan 2, an optical microscopy observation was made over a 30 s period. Between scan 2 and scan 3 the same observation was made over 60 s. Both observations showed the grain was unaltered.

Table 4: Relative intensities for various elements measured in natural samples.

	Ca	K	Cl	S	Si	Al	Mg	Na	F
E(keV)	3.69	3.31	2.62	2.31	1.74	1.48	1.25	1.04	0.67
I/Io V1 in the ice matrix	4.74	0.37	25.4	2.74	1.05	0.85	0.49	0.24	1.72
	1.30	***1.03***	***2.41***	***1.35***	***0.85***	***0.93***	***1.81***	***1.60***	***0.61***
I/Io V1 Aggregate Dark region	897	1950	27.9	757	277	45.9	31.0	2.32	5.51
	246	***5417***	***2.65***	***373***	***225***	***50.4***	***115***	***15.5***	***1.95***
I/Io V1 Inclusion	1.63	2.45	299	12.9	2.46	0.82	0.82	3.28	3.28
	0.45	***6.81***	***28.4***	***6.35***	***2.00***	***0.90***	***3.04***	***21.9***	***1.16***
I/Io V2 In the ice matrix	4.72	0.26	11.6	0.79	1.57	1.05	-	0.26	1.57
	1.30	***0.72***	***1.10***	***0.39***	***1.28***	***1.15***	***-***	***1.73***	***0.56***

Notes: The Energy (keV) corresponds to the Kα emission line. Relative intensity of signal (x 10^8), I/Io where I is the signal emitted by the element and Io the incoming intensity. In italic bold characters: ratio between the relative intensity and the background (as measured on artificial sample (Table 2)). Values lower than 2.0 are not considered significant. – signifies not detected

FIGURE CAPTIONS

Figure 1a: Internal part of the analysis chamber. (a) dewar (b) copper cylinder; (c) copper tress, (d) thermocouple, (e) support of piezometer electric scanner.

Figure 1b: The sample cell and its support. (a) the front window, (b) the sample cell support, (c) peek, (d) screw, (e) magnets.

Figure 1c: Details of the sample cell.

Figure 2: µXRF spectra from the sample cell filled with air and from the artificial sample (S1). The spectrum from the sample cell filled with air is characterized by a high peak from argon. This result shows the presence of air in the sample cell.

Figure 3a: µXRF spectra (Si Kα line only) from an inclusion observed on sample V2 (Vostok at 3572 m) for different radiation exposure times (2h30, 5h00 and 7h30).

Figure 3b: Relative intensity profiles from the Si Kα line along the cross section of an inclusion observed on sample V2 (Vostok at 3572 m) for different radiation exposure times (2h30, 5h00 and 7h30).
The absence of significant variations confirms the preservation of the sample, even after a long time exposure.

Figure 4a: Map of fluorescence yield of potassium (DC1 sample). Pixel size: 2.6 x 2.6 μm^2, integration time is 3.3s. Z1 scan refers to the A particle, Z2 to B, Z3 to C. K is found along the grain boundary (*gb*).

Figures 4b: Relative intensity profiles (Ca, K, S, Si, Al Kα line) along the cross section (Z1, Z2, Z3). Si and Al are highly concentrated on two specific spots (*A*) and (*B*). Si and Al could be within clay particles and associated with Ca (*A*), (*B*). S is associated with Ca in a highly concentrated spot (*A*).

Figure 5a: Aggregate observed on the V1 sample (Vostok at 3551 m). The lighter regions (visible at the periphery) may be gas bubbles while the dark regions look like the solid part of the aggregate. The region of interest on the picture was analyzed by µXRF (see Fig. 5b)

Figure 5b: Map of Ca and K distributed on the aggregate observed on sample V1(Vostok at 3551 m). 300 x 100 μm^2, pixel size: 1 x 1 μm^2, integration time 0.5 s. Ca is distributed as large particles. Their shapes and compositions are different inside (circles) and outside (dashed circle) the aggregate. Ca looks anti correlated with K (white circles).

Figure 5c: µXRF spectra from the upper particles inside (circles Fig. 5b) and outside (dashed circle).

Figure 6a: Map of S (Oxidized form) on the inclusion observed on sample V2 (Vostok at 3572m) using 2.482 keV, 50 x 40 μm^2, pixel size: 0.5 x 0.5 μm^2, integration time 0.5s.

Figure 6b: Map of S (Reduced form) on the inclusion observed on sample V2 (Vostok at 3572m) using 2.473 keV, 50 x 40 μm^2, pixel size: 0.5 x 0.5 μm^2, integration time 0.5s.

Figure 6c: Relative intensity profiles from the oxidized and reduced form of sulfur along the cross section of the inclusion observed on sample V2 (Vostok at 3572m)

Fig. 1a: Internal part of the analysis chamber.

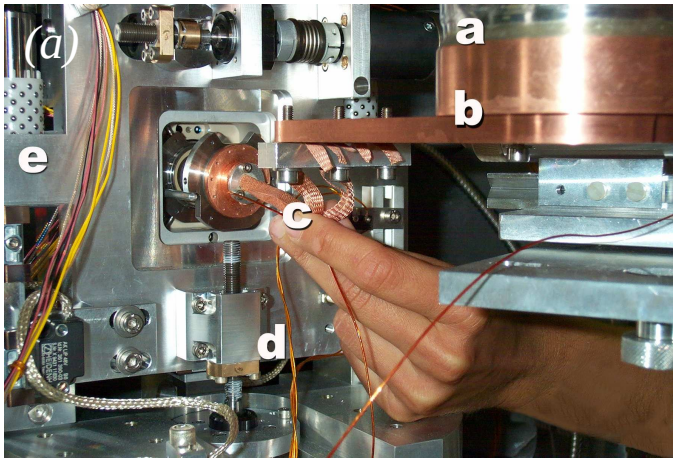

Fig. 1b: The sample cell and its support.

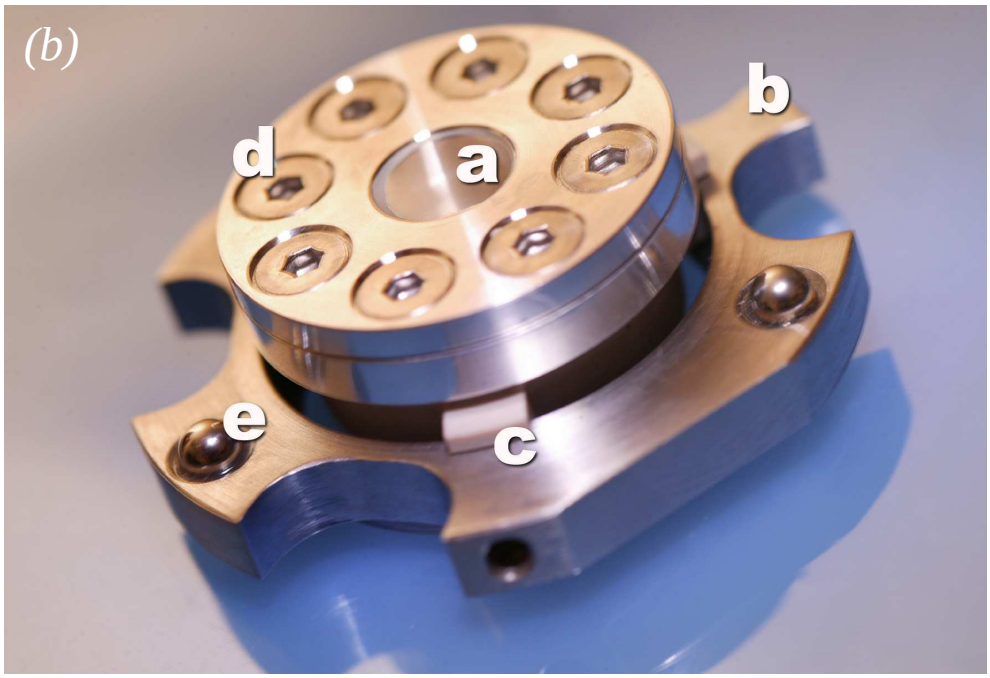

Fig. 1c: Details of the sample cell.

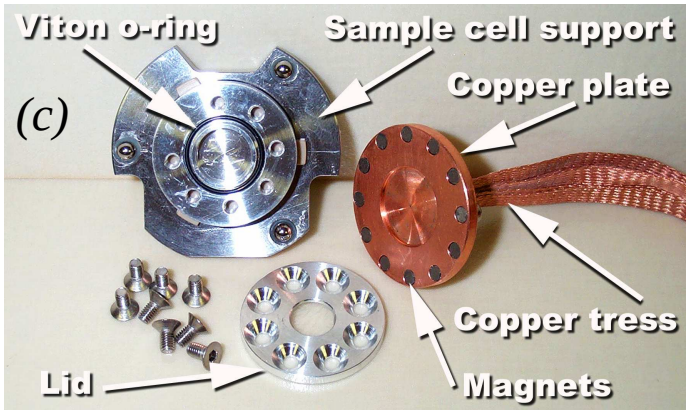

Fig. 2: µXRF spectra from the sample cell filled with air and from the artificial sample (S1)

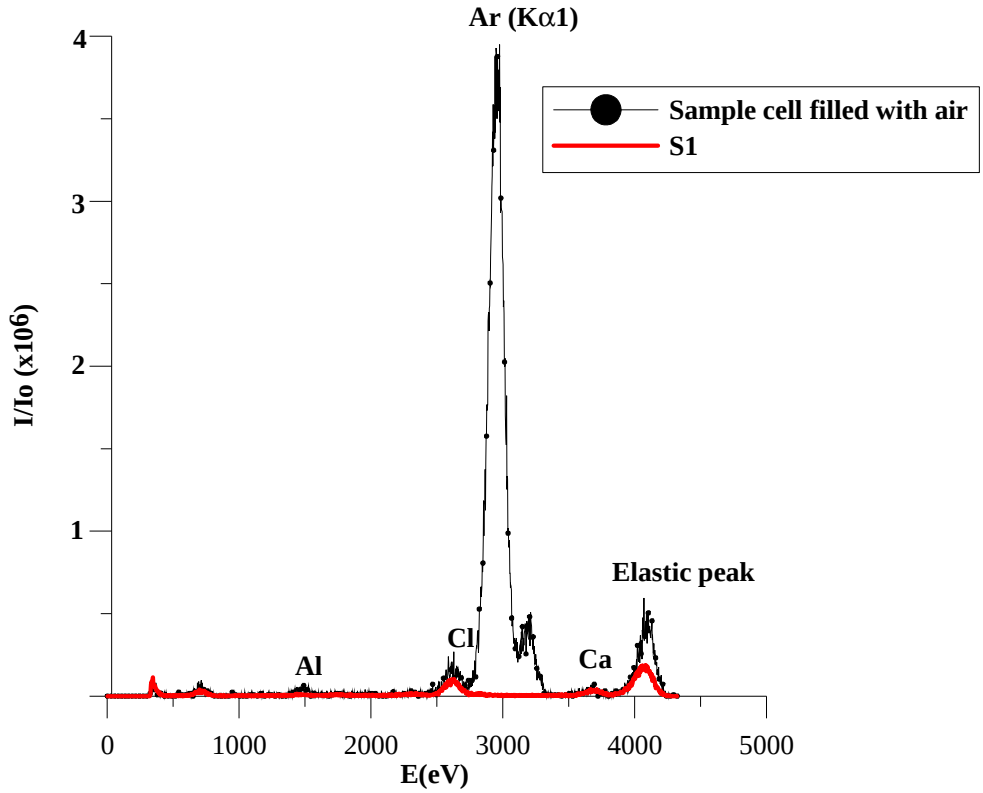

Fig. 3a: Comparison of μXRF spectra (only Si Kα line) from an inclusion observed on the sample V2 (Vostok at 3572 m) for different radiation exposure times (2h30, 5h00 and 7h30).

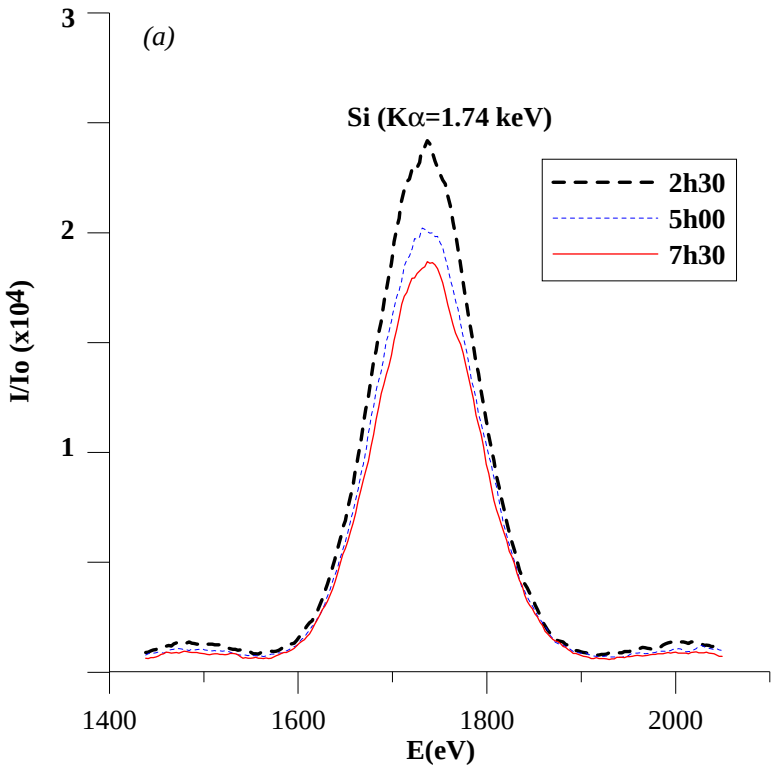

Fig. 3b: Relative intensity profiles (Si; Kα line) along the cross section of an inclusion observed on sample V2 (Vostok at 3572 m) for 3 different radiation exposure times (2h30, 5h00 and 7h30).

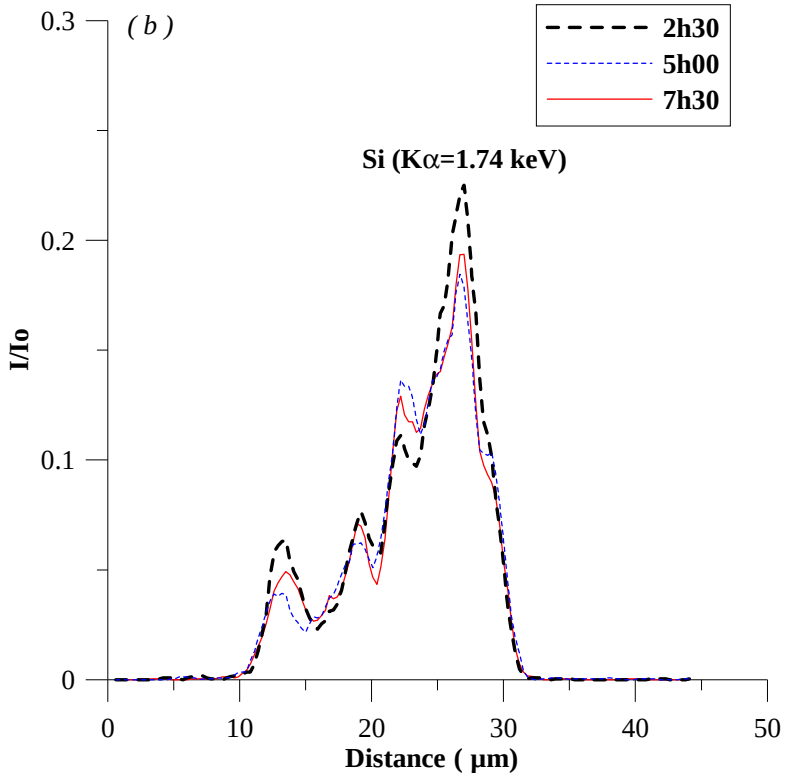

Fig. 4 a: Map of fluorescence yield of potassium (DC1 sample)

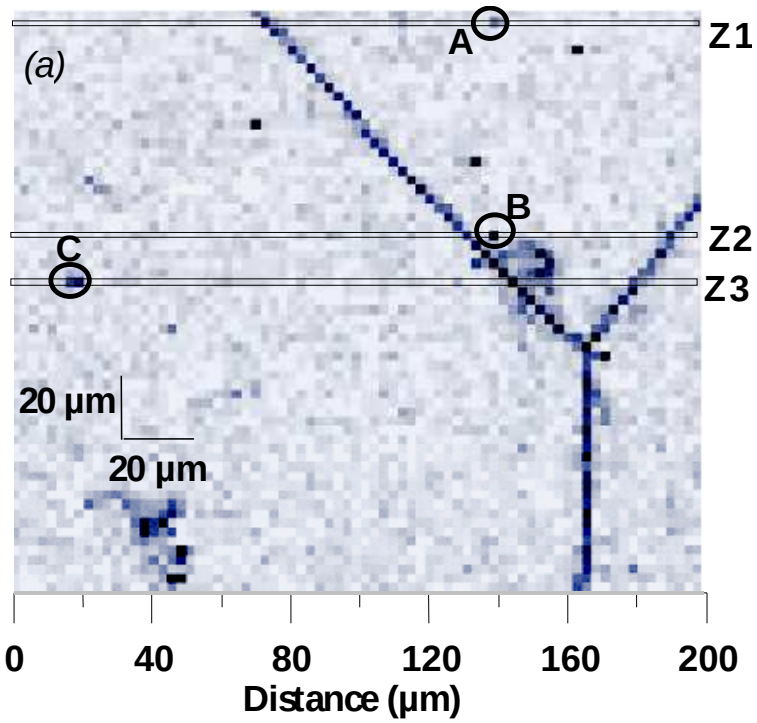

Fig. 4b: Intensity profiles (Ca, K, S, Si, A; Kα line) along the cross section (Z1, Z2, Z3).

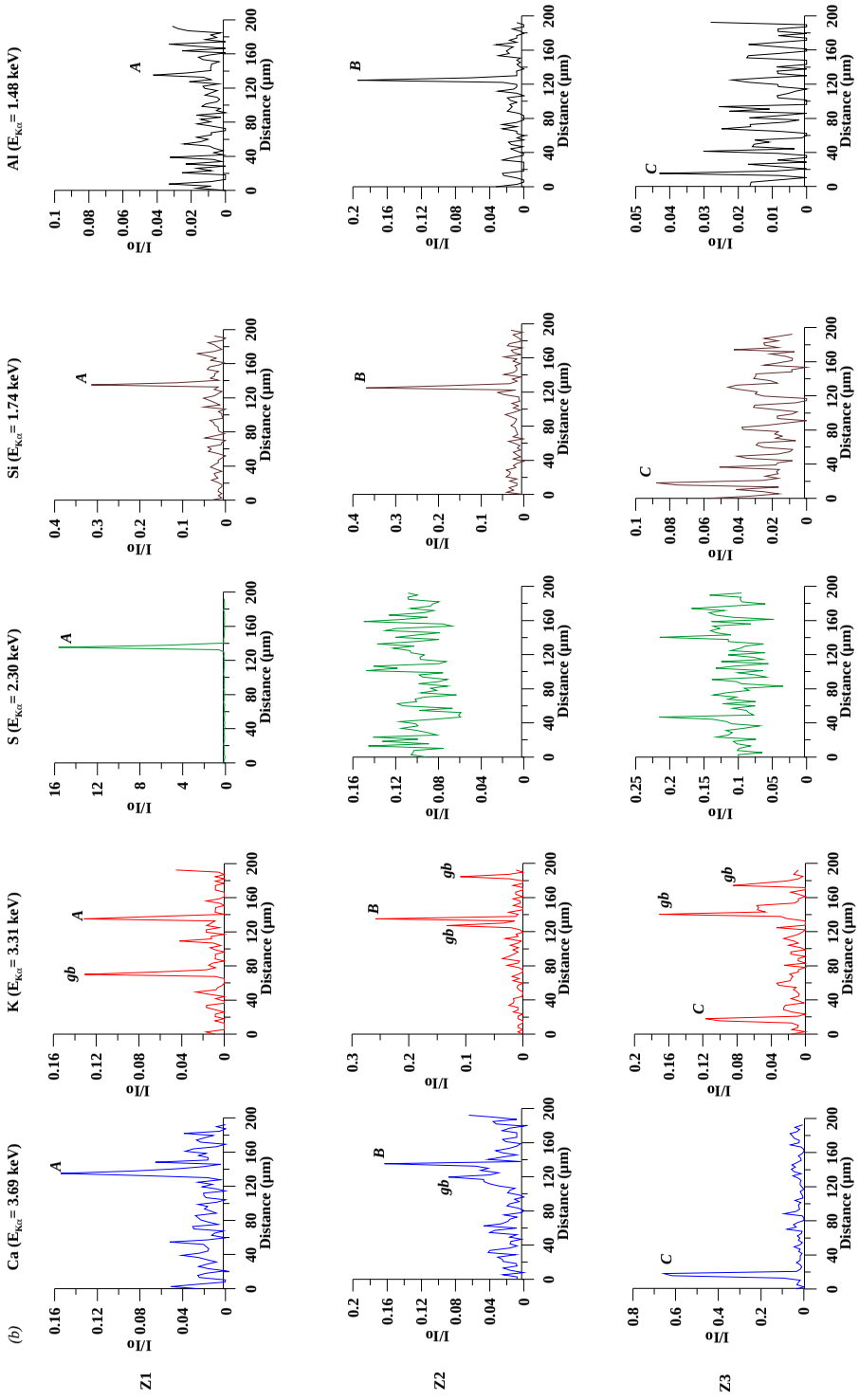

Fig.5a: Aggregate observed on the V1 sample (Vostok at 3551 m).

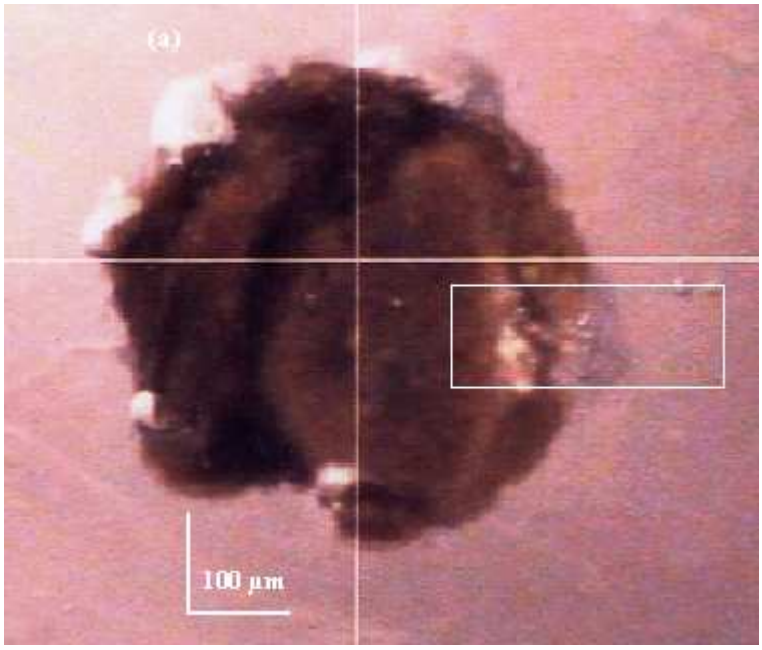

Fig. 5b: Map of Ca and K distributed on the aggregate observed on sample V1 (Vostok at 3551 m).

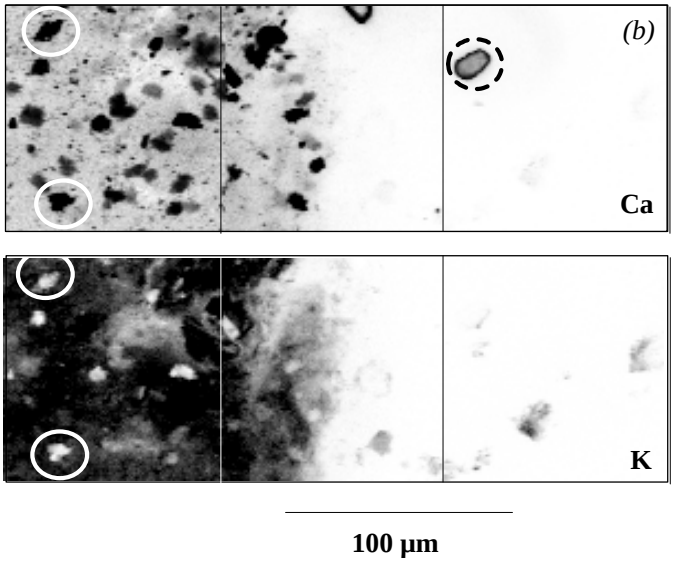

Fig. 5c: µX.R.F. spectra from the upper particles inside (circles Fig. 5b) and outside (dashed circle).

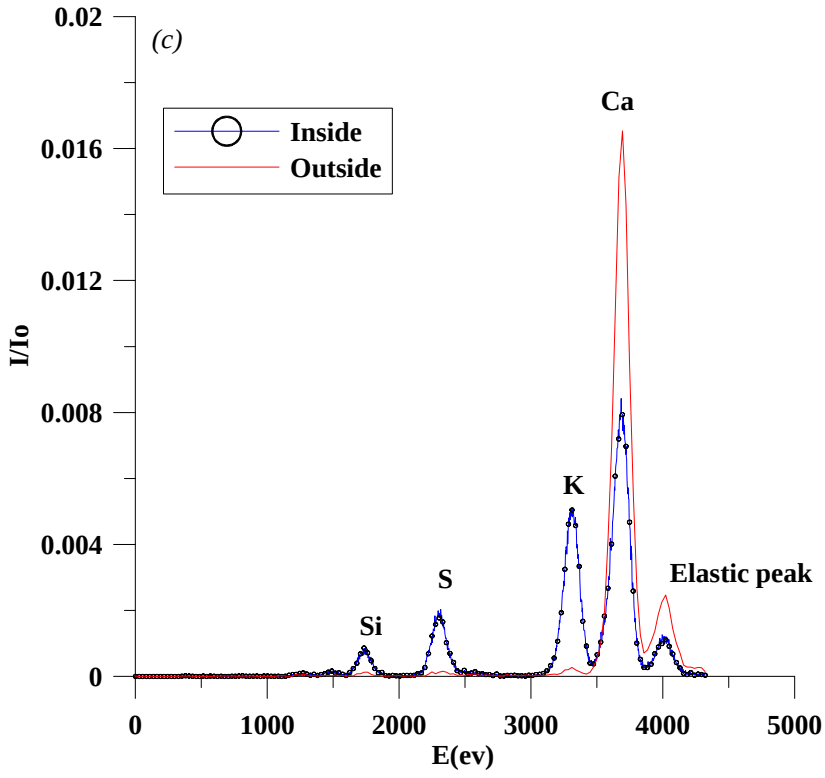

Fig. 6a: Map of S (Oxidized form) on the inclusion observed on sample V2 using 2.482 keV.

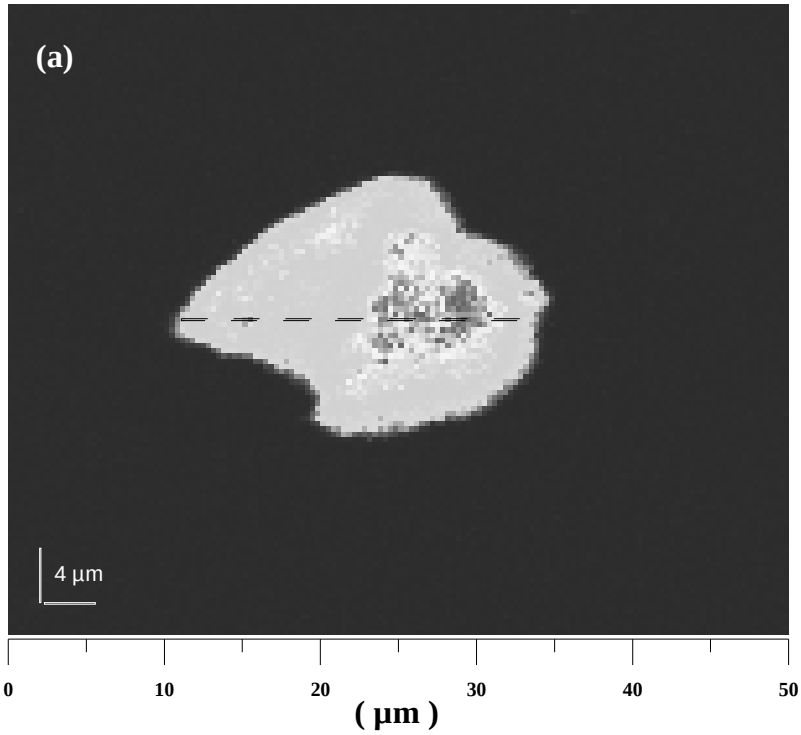

Fig. 6b: Map of S (Reduced form) on the inclusion observed on sample V2 (Vostok at 3572m) using 2.473 keV.

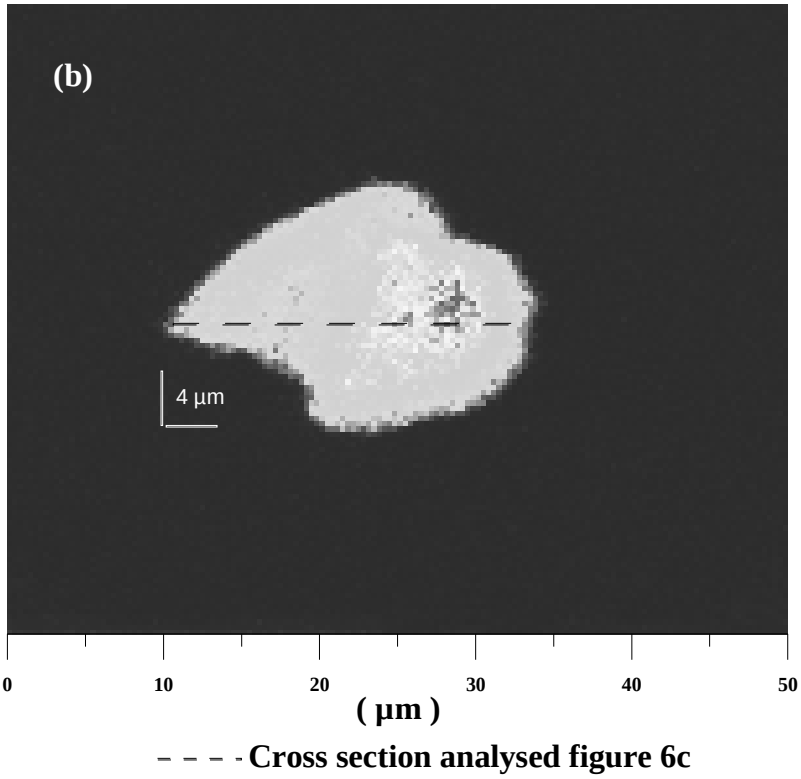

Fig. 6c: Relative intensity profiles from the oxidized and reduced form of sulfur along the cross section of the inclusion observed on sample V2 (Vostok at 3572m)